



Terahertz photonic integrated circuit for frequency tuning and power modulation

I. KUNDU,^{1,2,*}  J. R. FREEMAN,¹  P. DEAN,¹  L. H. LI,¹  E. H. LINFIELD,¹  AND A. G. DAVIES¹ 

¹*School of Electronic and Electrical Engineering, University of Leeds, Leeds, LS2 9JT, UK*

²*Currently with Optalysys Ltd., 8 Flemming Court, Wakefield, WF10 5HW, UK*

**I.Kundu@Leeds.ac.uk*

Abstract: The quantum cascade laser is a powerful solid-state source of terahertz-frequency radiation. However, integrating multiple photonic functions into a monolithic platform in this frequency range is non-trivial due to the scaling of photonic structures for the long terahertz wavelengths and the low frequency tuning coefficients of the quantum cascade lasers. Here, we have designed a simple terahertz-frequency photonic integrated circuit by coupling a racetrack resonator with a ridge laser in the longitudinal direction to design a notch filter. The transmission properties of this filter structure are dependent on the phase matching and losses in the coupled racetrack and results in a comb of stopband frequencies. We have optimized the comb separation by carefully selecting the cavity dimensions of the racetrack resonator to suppress longitudinal modes in the ridge laser enabling single-mode emission. The emission frequencies and output power from laser are controlled through appropriate control of drive currents to the ridge and the racetrack resonator. The emission frequency is electrically tuned over ~81 GHz exploiting Stark shift of the gain as a function of drive current at the ridge laser, coinciding with an output power variation of ~27% of the peak power (at a heat sink temperature of 50 K). The output power from the ridge also varied by ~30% and the frequency was tuned by a further 10 GHz when the driving conditions at the ridge laser are invariant and the current at the racetrack resonator was varied. To our best knowledge, this is the first report of a frequency engineering, tuning and power modulation of terahertz-frequency quantum cascade lasers using a photonic integrated circuit.

Published by The Optical Society under the terms of the [Creative Commons Attribution 4.0 License](https://creativecommons.org/licenses/by/4.0/). Further distribution of this work must maintain attribution to the author(s) and the published article's title, journal citation, and DOI.

1. Introduction

The quantum cascade laser (QCL) is a powerful solid-state source of terahertz (THz) frequency radiation, which has undergone rapid improvements since its first demonstration at THz frequencies in 2002 [1]. By means of bandstructure engineering and careful waveguide design, QCLs have been designed to lase at frequencies 1.2–5.6 THz [2,3], emit multi-Watts of output power [4] and can operate over a broad bandwidth exceeding 1 THz [5,6].

Notwithstanding these advantages, one of the major challenges for THz QCL technology has been the limited scope for integrating multiple photonic functions into a monolithically integrated platform. Photonic integrated circuits (PICs) are widely used in solid-state semiconductor lasers operating at the telecom wavelength of 1550 nm. A frequency tunable laser forms the core of different PIC designs. One of the first demonstration of the PICs is the multi-section sampled-grating distributed Bragg reflectors that are used to tune the emission frequency in telecom lasers [7]. Modern telecom PICs comprise of both active and passive sections and integrate photonic structures such as tunable lasers, modulators, arrayed waveguides and transceivers [8].

Integrating multiple photonic functions in the form of PIC at THz frequencies is non-trivial. For example, emission frequencies in semiconductor lasers are tuned by changing the refractive

index, either by varying the temperature of operation or through current induced Joule heating. However, the relative change of refractive index at THz frequencies is two orders of magnitude lower than telecom lasers and the temperature and current induced frequency tuning rates in THz QCLs are measured to be between 60–100 MHz/K and 5–8 MHz/mA [9]. Owing to this limitation, frequency tuning of THz QCLs has relied primarily on electro-mechanical mechanisms [10–12], the use of external cavities [13–15] or on deposition of dielectrics or condensation of gases in distributed feedback structures [16,17].

Another limitation of the THz QCL technology is the limited scope for modulation of output power. In telecom lasers, modulators are designed using a Mach-Zehnder interferometer and power is controlled through electro-optic effects. However, the long operating wavelengths at THz frequencies require impractically long cavity lengths to realize a Mach-Zehnder device. Instead, power modulation in THz QCLs has been demonstrated using, for example, mechanical modulators [18] and graphene based meta-materials in an external-cavity configuration [15]. The external cavity designs used in these designs are unsuitable for an integrated THz frequency PIC.

Nevertheless, recent reports of electrically-controlled frequency tuning exploiting Vernier selection [19–23], through use of aperiodic lattices [24] and by facet illumination [25,26] offer the advantage of system miniaturization, compact instrumentation and lay the foundation for designing a THz frequency PIC.

In this paper we report frequency engineering, electrically controlled tuning, and power modulation of THz QCLs using a simple PIC structure formed by coupling a racetrack resonator (RTR) with a ridge waveguide using a co-directional coupler. The resonant frequencies in the RTR are determined by phase matching conditions. At such resonant frequencies, the transmission through the ridge section can be completely extinguished by matching the round-trip losses in the RTR with the transmission through the coupler, resulting in the formation of a comb of stop-band frequencies. This coupled-RTR architecture is used extensively in telecom lasers and silicon photonics to design filters and modulators [27]. Although, the simplest implementations of this architecture are passive optical filters, integration of active components in RTRs has enabled frequency tuning of the filters. This has led to the development of power modulation techniques using a monolithic integrated photonic platform such as silicon based photonic technology for telecommunication applications.

Here we have developed an active coupled-RTR architecture for THz frequency QCLs. The operation and the device geometry are schematically illustrated in [Fig. 1(a) and 1(b)]. An RTR is coupled to a ridge laser in the longitudinal direction through evanescent field and forms a comb of stop band frequencies [shown as red bands in Fig. 1(a)]. The optical power at these resonant frequencies are fully confined to the RTR with negligible power transmitted through the ridge. We carefully select the lengths of the cavity sections such that the free spectral range (FSR) of the ridge laser is almost equal to the frequency separation between successive resonances in the RTR. That way, the optical power of most of the longitudinal modes in the ridge [shown as blue lines in Fig. 1(a)] are confined in both the RTR and the ridge laser, and emission is dominant at a single frequency. In this device, the ridge laser forms the primary active section and the RTR acts as both an active and a passive cavity. Frequency tuning through mode hops and power modulation is realized through precise control of current-induced changes in the refractive index in the ridge and the RTR, respectively.

The frequency tuning process with a passive RTR is illustrated in the top panel of Fig. 1(a). A change in the drive current in the ridge laser changes the FSR due to Stark shift of QCL gain and the resulting changes in refractive index arising from Kramer-Krönig relationship. This perturbs the overlap between the longitudinal modes and the stopband frequencies and emission frequency is shifted through careful adjustments in the ridge drive current. We report discrete mode-hops controlled by varying the drive current in just the ridge laser. In this case, the current amplitude in the ridge laser was restricted to ~50% of the dynamic range such that the output power varies by

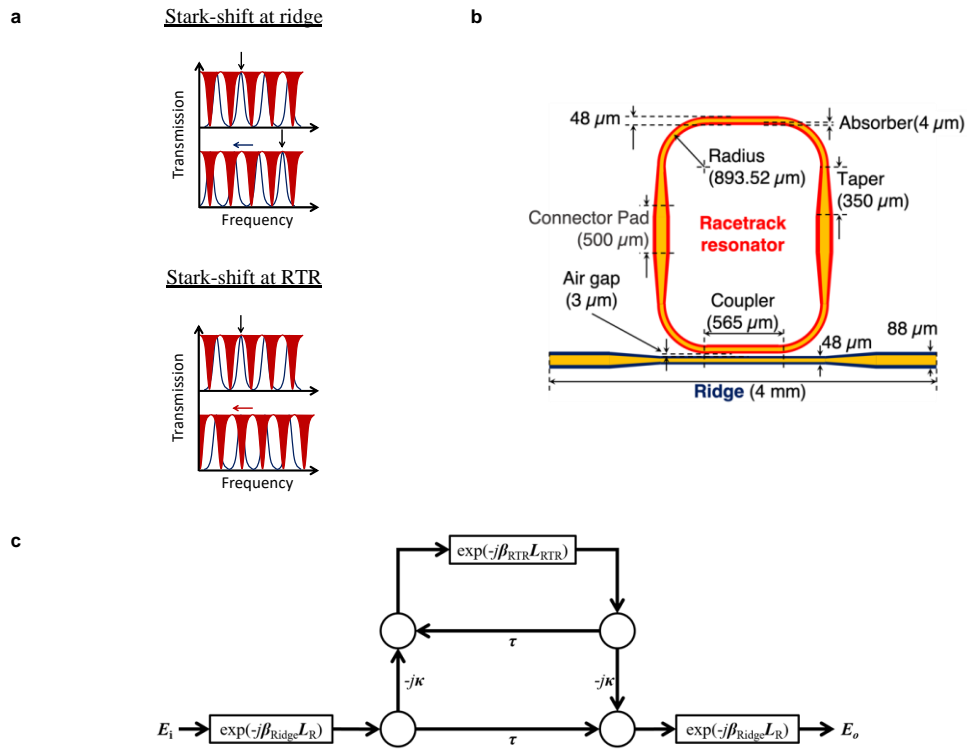


Fig. 1. Illustration of the operation, geometry and the signal flow graph for the coupled-RTR QCL. (a) A comb of stop bands formed by the RTR (red) is used to selectively suppress longitudinal modes of the ridge laser (blue), except the one marked with an arrow. (Top) Illustration of frequency tuning: a Stark-shift of the longitudinal modes in the ridge results in a mode-hop to higher frequencies. (Bottom) Illustration of power modulation: a red-shift in the stop bands combs results in suppression of longitudinal modes and reduces the output power. (b) A ridge section (blue) is coupled to a RTR (red) using a 48- μm -wide coupler section. Wider cavity sections (88- μm -wide) are used for wire bonding and are connected to the narrow waveguide sections through a 350- μm -long taper section. A 4- μm -wide absorber is used throughout to suppress higher order transverse modes. The transmission properties through the coupled-RTR device is controlled through appropriate selection of the lengths of the ridge, coupler, air gap and RTR (radius of the RTR arcs); and are selected to be 4 mm, 565 μm , 3 μm and 9.144 mm (radius = 893.52 μm) respectively. (c) Unidirectional signal flow graph for the coupled RTR device. The propagation through the ridge is modelled as two paths of equal lengths, $L_R = L_{\text{Ridge}}/2$; where L_{Ridge} is the total length of the ridge.

a maximum of 30% of the peak power. We have experimentally measured single-mode emission between ~ 3.358 – 3.439 THz from a fabricated device, when the drive current in the ridge was varied in the range ~ 1.1 – 2.1 A and at a constant heat sink temperature of 50 K.

The output power from the ridge laser is modulated by driving an electric field across the RTR to change the overlap between the longitudinal modes and the stopband frequencies [illustrated in the bottom panel of Fig. 1(a)]. The stopband frequency combs are red-shifted through precise control of the RTR drive current. An increase in the overlap between the ridge modes and the stopbands decrease the optical power from the ridge (when the drive current to the ridge are invariant). The RTR also acts as a phase filter when it is biased just above threshold. The red-shift

of the comb and the phase filtering capability of the RTR was exploited to demonstrate a power modulation scheme when the drive conditions across ridge laser were invariant. In this way we have measured a change in the output power from the ridge laser by $\sim 30\%$, along with a tuning of the emission frequency by a further 10 GHz, when the drive current through the RTR was varied in the range ~ 0 –1.6 A.

2. Device design

A coupled-RTR device was designed with a THz QCL active region and a metal-metal waveguides [28], shown in Fig. 1(b). The device comprises a ridge section separated from a RTR by an air-gap. A portion of the ridge and the RTR were designed to run parallel to each other forming a longitudinal coupler, where the THz electric field can couple evanescently between the two sections.

In order to preserve the fundamental transverse mode, a narrow waveguide of width $48\ \mu\text{m}$ was used for both the ridge and the RTR to form the coupler section. To facilitate electrical wiring without damaging the ridge, a wider waveguide ($88\ \mu\text{m}$) was used on either side of the coupler. A $350\text{-}\mu\text{m}$ -long impedance matching taper connects the $48\text{-}\mu\text{m}$ -wide and the $88\text{-}\mu\text{m}$ -wide waveguides [21]. Similarly, two $88\text{-}\mu\text{m}$ wide waveguides of length $500\ \mu\text{m}$ were incorporated symmetrically into the RTR via impedance matching tapers to enable electrical connections to be formed. A $48\text{-}\mu\text{m}$ -wide narrow waveguide of the same length as the coupler was used to form the top of the RTR, also to preserve the symmetry. The rest of the RTR was formed by designing four $48\text{-}\mu\text{m}$ -wide arcs. A $4\text{-}\mu\text{m}$ -wide absorber was employed on either side of the top metal cladding across the entire device to suppress higher order transverse modes [29]. The length of the ridge section was selected to be 4 mm.

3. Operating principle

The operating principle of the coupled-RTR structure is explained using a single-pass unidirectional transmission of the electric field. The signal flow graph for the device is shown in Fig. 1(c). The propagation through the ridge is modelled as two separate regions; before and after the coupler section. To maintain symmetry, the lengths of these propagation paths are designed to be equal, $L_R = L_{\text{Ridge}}/2$; where L_{Ridge} is the length of the ridge. A fraction of the input electric field (E_i) is transmitted through the ridge and the rest is coupled to the RTR, the magnitude of which are determined by the transmission (τ) and coupling (κ) coefficients of the coupler section, respectively. The coupled field propagates through the length of the RTR (L_{RTR}). A fraction of this field is coupled back into the ridge through the same coupler section, where it combines with the transmitted input field and propagates through the remainder of the ridge. The remainder is transmitted through the RTR, forming a loop.

The transfer function of this system is derived using Mason's rule [30], used extensively to model control systems. The output electric field (E_o), normalized to the input electric field, can be expressed through the following frequency dependent transfer function [8]:

$$H = \tau \exp(-j\beta_{\text{Ridge}}L_{\text{Ridge}}) - \frac{\kappa^2 \exp(-j\beta_{\text{RTR}}L_{\text{RTR}}) \exp(-j\beta_{\text{Ridge}}L_{\text{Ridge}})}{1 - \tau \exp(-j\beta_{\text{RTR}}L_{\text{RTR}})} \quad (1)$$

where β_{Ridge} and β_{RTR} are the complex propagation constants in the ridge and the RTR. The coupling coefficient into the RTR is expressed as:

$$\kappa^2 = \sin^2(KL_C) \quad (2)$$

where L_C is the length of the coupler, $K = (\beta_s - \beta_a)/2$ is the coefficient of coupling and is related to the propagation constants of the symmetric (β_s) and anti-symmetric modes (β_a) in the coupler. For loss-less coupling, the transmission through the coupler is $\tau = \sqrt{1 - \kappa^2}$.

The complex propagation constants in the ridge and the RTR are calculated using the expression:

$$\beta = \frac{2\pi\nu}{c}n_{\text{eff}} + j(G - \alpha) \quad (3)$$

where n_{eff} is the effective refractive index, ν is the frequency, G is the gain and α is the total loss.

The filter characteristics of the coupled-RTR are determined by the zeros of the denominator in the transfer function H . The RTR is resonant at frequencies ν when the round-trip phase contribution is an integer multiple of 2π , i.e. $\exp(j2\pi\nu n_{\text{eff}}L_{\text{RTR}}/c) = 1$. At such resonant frequencies, the output electric field E_o is completely extinguished if the round-trip losses in the RTR equal the transmission through the coupler, i.e. when $\exp[(G_{\text{RTR}} - \alpha_{\text{RTR}})L_{\text{RTR}}] = \tau$. This condition is described as ‘critical coupling’ and the device acts like a notch filter forming a comb of stop bands. Unlike the ridge laser (a Fabry-Pérot resonator) whose FSR is inversely proportional to $2 \times L_{\text{Ridge}}$, the RTR does not have facets and forms a closed loop. As such, the FSR of the RTR is inversely proportional to L_{RTR} . The frequency separation or FSR between successive resonances in the RTR is calculated from the group refractive index (n_g) using the expression $\text{FSR}_{\text{RTR}} = c/(n_g L_{\text{RTR}})$. In order to match the FSR in the RTR to that in the ridge, the length of the RTR is approximately twice the length of the ridge. The RTR also acts as a phase filter at a resonant frequency ν if the gain cancel the round-trip losses, i.e. when $\exp[(G_{\text{RTR}} - \alpha_{\text{RTR}})L_{\text{RTR}}] = 1$. In this condition, the output electric field E_o acquires a π -phase shift.

We have exploited the stopband or notch filter characteristics of the RTR to suppress most longitudinal modes and to demonstrate emission predominantly at a single frequency (with spurious side modes). The lengths of the cavity sections were carefully selected to form critical coupling and such that the FSR of the RTR is slightly smaller than that of the ridge. This ensures suppression of most of the longitudinal modes in the ridge such that most of the output optical power is at a single dominant frequency. The material gain and Stark shift was then exploited to tune the emission frequency.

Finite element modelling (FEM) techniques have been used to select the length of the coupler section and to determine the total length of the RTR, through a systematic study of the radii of the arcs. Then, the transmission of the optical field through the device was simulated using both FEM and an analytical model using transfer matrices.

3.1. Finite element modelling

Optical modes and unidirectional propagation of the electric field in the coupled-RTR was simulated via FEM, using COMSOL Multiphysics software. Initially, the propagation of the electric field through a longitudinal coupler was simulated at different air-gap separations to calculate propagation constants of the symmetric and the anti-symmetric modes and the length of the coupler section. An air gap with a width of $3 \mu\text{m}$ was selected as a best compromise for efficient coupling (reducing the length of the coupler section) whilst ensuring an electrical isolation between the ridge and the RTR. In this case, the propagation constants of the symmetric and the anti-symmetric modes were computed to be $\beta_s = 256.070 \text{ rad/mm}$ and $\beta_a = 254.630 \text{ rad/mm}$ respectively, and the coefficient of coupling was calculated to be $K = 0.72 / \text{mm}$ for the two $48\text{-}\mu\text{m}$ -wide cavity-sections.

Because of the interdependency of the coupling, transmission and loss coefficients, and their dependence on the device geometry, a number of realistic coupling coefficients were investigated as potential starting points. Starting with $\kappa = 0.4$ and assuming loss-less coupling, the transmission through the coupler was calculated to be $\tau = 0.92$. In order to achieve critical coupling, the total loss in the RTR was calculated to be $\sim 9.97 \text{ cm}^{-1}$. The radii of the arcs in the RTR were varied systematically using FEM to minimize the length of the RTR and to ensure that the round-trip losses roughly equal τ . An Eigen frequency solver was used to calculate the

losses in the RTR. A loss of $\sim 10 \text{ cm}^{-1}$ was calculated for an RTR with a coupler length $L_C = 565 \text{ }\mu\text{m}$ and an arc radius of $r = 893.52 \text{ }\mu\text{m}$. In this case, the length of the RTR is calculated to be 9.144 mm . The coupling coefficient of this RTR was calculated to be $\kappa = 0.396$, close to the initial approximation of 0.4.

The resonant frequencies in this coupled-RTR device were simulated via a unidirectional propagation of the electric field at a constant electric field of 8 kV/cm applied across the ridge and at different electric fields across the RTR, as we show in Dataset 1 (Ref. [31]) and Fig. 2(a). A frequency comb of band-stop filters was obtained from the simulations, where the electric field was almost completely confined in the RTR with negligible transmission through the ridge. Increasing the field across the RTR red-shifts the comb of stop band frequencies due to changes in the refractive index. The refractive index change was obtained experimentally, from a reference ridge waveguide device.

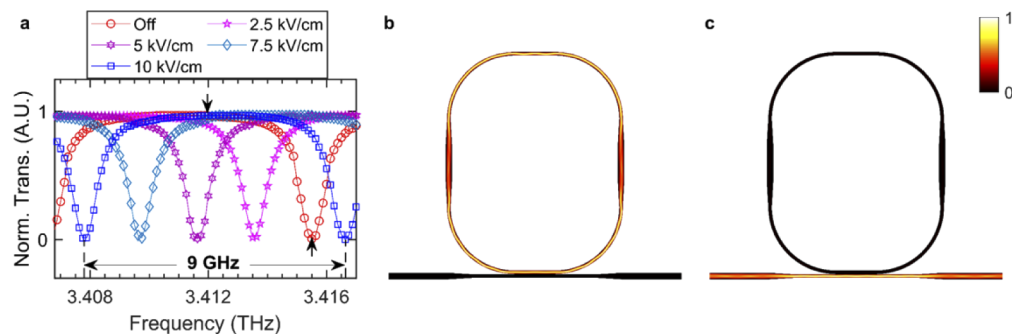


Fig. 2. Simulation of electric field propagation through the coupled-RTR QCL, computed using a finite element model. (a) Normalized transmission (E_o/E_i) through the device when the ridge is applied with 8 kV/cm and at different bias fields across the RTR. A comb of band stop filters with an FSR of 9 GHz is predicted. An increase in the electric field across the RTR results in a red-shift of the combs. The power distribution in the device at a resonant and a non-resonant frequency (marked with an arrow) is shown in b, c, when the RTR is switched off. (b) Power distribution at a resonant frequency of $\sim 3.4155 \text{ THz}$, where the electric field is almost fully confined in the RTR; and (c) at a non-resonant frequency $\sim 3.412 \text{ THz}$, where the field is almost fully transmitted through the ridge.

The FSR of the resonances is calculated to be $\sim 9 \text{ GHz}$, slightly smaller than the FSR of $\sim 10.5 \text{ GHz}$ measured experimentally from a 4-mm -long reference device (without any RTR). The power distribution at a resonant frequency of $\sim 3.4155 \text{ THz}$ is shown in Fig. 2(b) where the field is fully confined in the RTR. To illustrate a transmission through the ridge at other non-resonant frequencies, the power distribution through the device at $\sim 3.412 \text{ THz}$ is also shown in Fig. 2(c).

The FEM model does not account for changes in refractive index due to Kramer–Krönig relationship or any feedback from cavity facets. Instead, an analytical model was used to include these effects and to predict the emission frequencies and output power from the device.

3.2. Analytical modelling using transfer function

An analytical model based on the transfer function description of the coupled-RTR (H) was used to simulate the emission spectra from the device. The model accounted for feedback from the cleaved facets in the ridge and is similar to the transfer matrix model of a Fabry–Pérot laser [8]. Here we replace the propagation path of the Fabry–Pérot laser with the uni-directional single pass transfer function H . The transfer function H was used to simplify the signal flow graph for the complete device [Fig. 3(a)]. The facets of the ridge were treated as two ports. The coefficients of reflection (r) at each port are identical. For a loss-less coupling, the output electric field (E_o) is

related to the input field (E_i) through the following expression (derived using Mason's rule):

$$S_{21} = \frac{E_o}{E_i} = \frac{t^2 H}{1 - r^2 H^2} \quad (4)$$

where t is the coefficient of transmission.

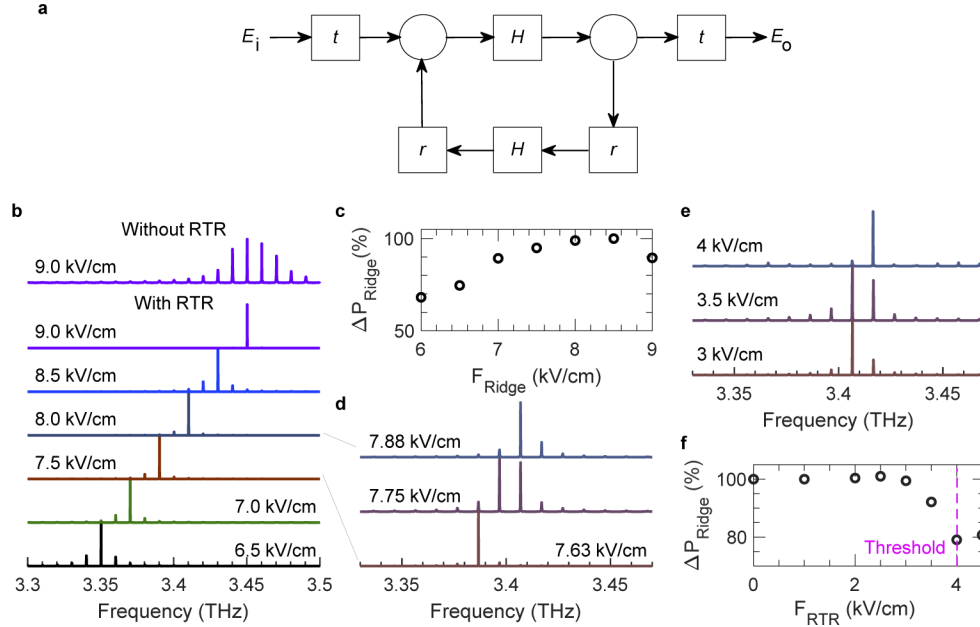


Fig. 3. Signal flow graph of the complete device and results from analytical simulations.

(a) Simplified signal flow graph for the complete device including the effects of feedback from as-cleaved facets in the ridge. H is the transfer function describing unidirectional propagation through the coupled-RTR. (b) Simulated transmission peaks as a function of electric field applied across the ridge (F_{Ridge}), when the RTR is not driven electrically and acts as a passive resonator. Mode hops separated by ~ 20 GHz is predicted when the electric field is coarsely varied between 6.5–9.0 kV/cm in steps of ~ 0.5 kV/cm. The transmission peaks from the ridge without any coupled RTR is also shown for comparison, when $F_{\text{Ridge}} = 9$ kV/cm. (c) Change in output power (ΔP_{Ridge}), normalized to the peak power, as a function of F_{Ridge} . (d) For small changes in the field < 0.3 kV/cm, the emission is predicted to change from single-mode to multiple longitudinal modes, shown when F_{Ridge} is varied between 7.63–7.88 kV/cm. (e) Transmission peaks as a function of electric field applied across the RTR (F_{RTR}). The electric field across the ridge is maintained at 7.75 kV/cm and that across the RTR is varied between 3–4 kV/cm (below the lasing threshold of the RTR). (f) Change in output power (ΔP_{Ridge}), normalized to the peak power, as a function of F_{RTR} .

The model included frequency dependent material gain as a function of drive current and heat sink temperatures; with contributions from the Stark shift of gain and dispersion of the refractive index arising through Kramer–Krönig relationship [32]. The Stark shift was calculated from the applied electric field across the QCL using the expression [33]:

$$\Delta E_S = eF (\langle \Psi_2 | z | \Psi_2 \rangle - \langle \Psi_1 | z | \Psi_1 \rangle) \quad (5)$$

where Ψ_2 and Ψ_1 are the wavefunctions of the upper and lower laser levels and e is the elementary charge. The total Stark shift of the QCL material was calculated to be $\Delta E_S = 2.64$ meV and its variation as a function of electric field was calculated to be $dE_S/dV = 0.504$ meV/V [21].

In order to ensure that the output power varies less than 25% of the peak power, the electric field across the ridge was varied in the range $\sim 6.5\text{--}9\text{ kV/cm}$, although the dynamic range in reference devices was measured to be $\sim 4\text{--}12\text{ kV/cm}$. The emission frequencies and changes in output power simulated as a function of electric field across the ridge is shown in Fig. 3(b) (when the RTR acts as a passive cavity). The filter characteristics of the RTR enable suppression of most of the longitudinal modes in the ridge, favoring emission dominantly at a single frequency with spurious power in the neighboring modes. A red-shift of the longitudinal modes is predicted exploiting Stark shift of the gain spectrum [21] resulting in mode-hops with a blue-shift in frequencies with increasing applied fields. The electric field across the ridge was carefully varied in steps of 0.5 kV/cm such that the emission modes hop to the alternate longitudinal modes, i.e. frequencies tune discretely in steps of $\sim 20\text{ GHz}$. The transmission properties without any RTR was also calculated for comparison. A multi-mode emission was predicted in this case. The emission frequencies simulated when an electric field of 9 kV/cm was applied across the ridge (without any RTR) is also shown in Fig. 3(b).

A frequency tuning range of $\sim 100\text{ GHz}$ and a change in output power of $\sim 25\%$ [Fig. 3(c)] is predicted from the coupled-RTR device when the electric field across the ridge is varied in the range $\sim 6.5\text{--}9\text{ kV/cm}$.

We note that the side-mode suppression is sensitive to small changes in the electric field across the ridge. For changes less than 0.3 kV/cm the suppressions are disrupted and emission at multi-modes are predicted. This is shown in Fig. 3(d), where the transmission from the device is simulated at electric fields $7.63\text{--}7.88\text{ kV/cm}$. The single mode emission at 7.63 kV/cm is disrupted to favor emissions at multiple longitudinal modes, when the field is increased to 7.75 kV/cm . A further increase in the field to 7.88 kV/cm increases the side-mode suppression and blue-shifts the dominant emission frequency. The precise control of ridge bias required to obtain a high spectral purity is not surprising. Passive filters using micro ring resonators and RTRs used in silicon photonics are known to be sensitive to ambient temperatures and suffer from shifts in resonant frequency with small changes in thermal drifts.

In such multi-mode driving conditions of the ridge, the single-mode emission can be restored by driving the RTR with small sub-threshold currents to shift the comb frequencies. This is shown in Fig. 3(e), where multi-mode emission (simulated at a field of 7.75 kV/cm across the ridge) is disrupted to restore single-mode emission by driving the RTR at 3 kV/cm . An increase in the field to the threshold (4 kV/cm) also results in a mode-hop to an adjacent longitudinal mode.

We note that increasing the electric field to the threshold nullifies the total losses in the RTR. The resulting change in the phase of the resonant frequencies at threshold reduces the output power from the ridge. A variation in the output power due to an increase in drive field across the RTR is shown in Fig. 3(f). The output power, calculated by summing optical power at all frequencies, is predicted to reduce by $\sim 20\%$ when the RTR field is increased from $2.5\text{--}4.5\text{ kV/cm}$. This reduction in output power coincides with the frequency tuning shown in Fig. 3(e). Active RTRs and micro-rings are used extensively to modulate power in diode lasers. However, unlike the present geometry, in such implementations the ridge acts as a passive cavity and is illuminated with single-mode light from an external source.

4. Results

A THz QCL, based on the active region design reported in [34], was rescaled to operate at frequencies $3.3\text{--}3.5\text{ THz}$ and was grown using molecular beam epitaxy using GaAs/ $\text{Al}_{0.18}\text{Ga}_{0.82}\text{As}$. The active region comprising of 115 repetitions of alternating layers of $\text{Al}_{0.18}\text{Ga}_{0.82}\text{As}$ (barrier)/GaAs (well) were grown on a GaAs substrate in the sequence: $3.8/14.2/2.9/16.3/2.9/6.8/2.9/8.2/2.9/9.1/2.9/11.3/1.9/12.9/11.2.6/0.5/10.8\text{ nm}$ (barriers in italics). The 16.3 nm -wide well was n -doped with Si at $3 \times 10^{16}\text{ cm}^{-3}$. The QCL with RTR was fabricated with metal-metal waveguides and

was characterized in pulsed mode (2- μ s-wide pulses, 10 kHz) at a heat sink temperature of 50 K. The device was not tested in continuous wave mode due to limitations imposed by fabrication imperfections.

The light-current-voltage characteristics from the device were measured by driving the ridge section only with a passive RTR (unpowered). The field across the QCL was calculated by normalizing the measured voltage with the thickness of the device (14.33 μ m). The threshold current (density) of the device was measured to be \sim 400 mA (\sim 160 A/cm²) at a terminal of \sim 6 V (field \sim 4.2 kV/cm). A peak power of \sim 2.75 mW was measured when the drive current (density) was increased to \sim 2.10 A (\sim 580 A/cm²) at a terminal voltage of \sim 12 V (field \sim 8.4 kV/cm), as shown in Fig. 4(a).

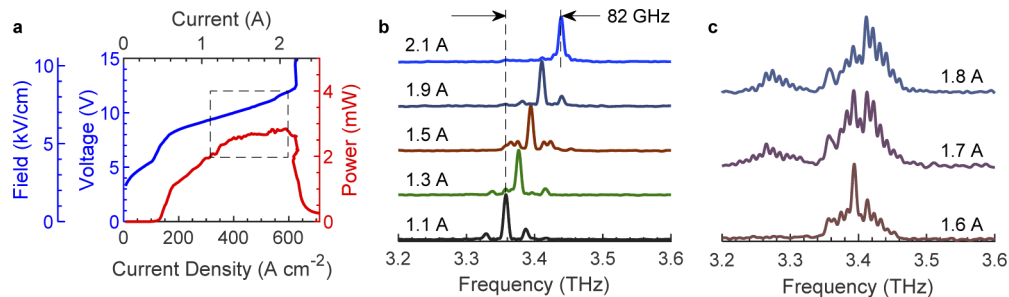


Fig. 4. Experimental data measured at a heat sink temperature of 50 K when the RTR is switched off and acts as a passive cavity. (a) Light-current/current density-voltage measured by varying the drive current in the ridge. The operating regime used to measure the spectra from the device is marked using a dashed rectangle. (b) Normalized intensity of the spectra measured at different drive currents such that the laser operates at a single frequency. (c) Normalized spectra showing emission at multiple longitudinal modes in the ridge, arising due to misalignment of stopband combs with the longitudinal modes. Spectra are offset for clarity.

Emission frequencies were measured using a Bruker Fourier transform infrared spectrometer with a frequency resolution of 7.5 GHz. Spectra were recorded at drive currents 1.10–2.10 A (when the output power varied by \sim 27%, i.e. between \sim 2–2.75 mW). A single-mode emission at \sim 3.358 THz was measured at a drive current of 1.10 A which blue-shifted due to Stark shift of gain as the drive current in the ridge was increased. The single-mode emission is due to an alignment of the RTR stopband comb with the longitudinal modes at the ridge and the resulting suppression of the longitudinal modes. Small changes in the drive current (by \sim 100–150 mA) disrupted this comb alignment and emission reverted back to multi-modes. A further increase in the drive current by another \sim 100–150 mA restored single-mode and resulted in a mode-hop due to a blue-shift of the resonant frequency. This way, mode hops between \sim 3.358–3.439 THz (in steps of \sim 20 GHz) was measured as the drive current was increased to 2.10 A (in steps of \sim 200–300 mA), as shown in Fig. 4(b). The emission frequencies are in close agreement with the simulated values and the difference of \sim 7 GHz between the experimental and simulated frequencies arise due to the slight difference in refractive index in the experimental and simulated device and fabrication tolerances.

Multi-mode emission resulting from a disruption of the comb alignment is shown in Fig. 4(c), measured at drive currents of \sim 1.60–1.80 A supplied at the ridge and with a passive RTR. The ridge emits at multiple frequencies and the spectra from the device resembles that of a Fabry-Pérot laser, when the RTR is not resonant at the ridge longitudinal modes (for e.g. at a drive current of 1.7 A). Close inspection of the spectra reveals emission on multiple longitudinal modes supported by the ridge section, as predicted in the simulations.

The effect of a misalignment of the RTR stopband comb was also evaluated by electrically driving the RTR, when the current amplitude in the ridge was maintained at 2.10 A. An increase in the RTR current to the threshold current of ~ 1 A resulted in a gradual degradation of side-mode suppression and eventually to multi-mode emission [Fig. 5(a)], as predicted in the simulations. This also coincided with a reduction in the output power by $\sim 20\%$ from 2.75 mW to 2.2 mW [Fig. 5(b)]. The reduction in the output power close to RTR threshold is due to a $\sim \pi$ -shift in phase acquired in the RTR, which results in a destructive interference between the optical field in the RTR and the ridge.

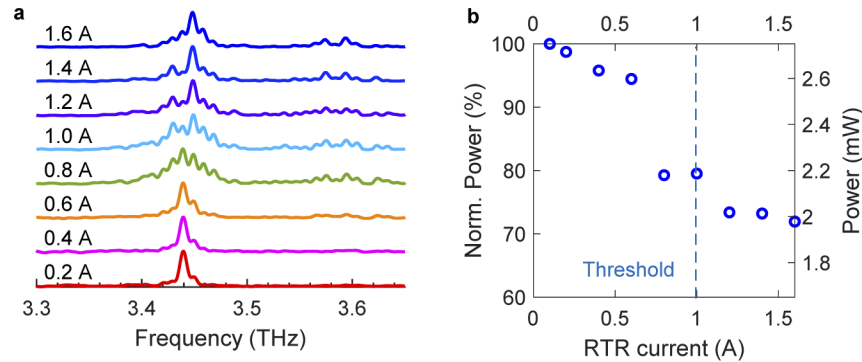


Fig. 5. Experimental data measured at a heat sink temperature of 50 K when the drive current through the RTR is varied and the ridge is driven at a constant drive current of 2.1 A. (a) Normalized spectra at different drive currents (offset for clarity). (b) Variations in the output power from the ridge (absolute value and normalized with peak power expressed in percent) as a function of the drive current in the RTR.

A further increase in the RTR drive current to 1.6 A resulted in a mode hop to ~ 3.449 THz. The total tuning range from the device is measured to be ~ 91 GHz. Emission at multiple frequencies centered at ~ 3.6 THz is recorded when the RTR drive current > 0.8 A (transparency/above threshold). Emission at these frequencies were observed from reference devices (without RTR) when the drive current densities are > 600 A/cm², i.e. operating at the negative differential resistance regime. The activation of these frequencies when the ridge is driven at a constant bias of 2.1 A (just below the negative differential resistance regime) and the RTR is at transparency/above threshold is due to cavity pulling effects [21]. Although the output power was predicted to increase slightly (by 1%) at drive currents just above threshold [Fig. 3(f)], a reduction in output power by $\sim 8\%$ to ~ 2 mW was measured experimentally.

This disagreement between the experimental and simulated results may arise due to the assumption of loss-less coupling in the coupler section. A lossy coupling scatters a portion of the optical field incident at the coupler into the RTR forming a backward mode propagating in the clockwise direction, which then couples with the forward mode emanating from coupling in the counter-clockwise direction. Nevertheless, the simple model accurately predicts device behavior at sub-threshold currents in the RTR and the experimental measurements are in good agreement with simulated predictions in Fig. 3.

At threshold, the phase of the resonant frequencies in the RTR acquire a π -shift. As a result, the optical field in the device interfere destructively, the effects of which also depends on the coupling between the forward and backward mode. Similar destructive interference of optical field due to π -shift in phase is exploited to design optical modulators using Mach-Zehnder interferometers. The reduction in output power of the single mode beyond the RTR threshold measured here suggests the effect of this destructive interference between forward and backward modes due to a π -phase shift. This effect can be exploited further to design THz modulators

by merging the present RTR design with two Y-branches to form an interferometer. We note that modulators using such an RTR-Y-branch geometry will require threshold currents in the RTR section increasing the electrical power budget, however these structures have tremendous possibility for the development of a monolithic platform, without the need for external modulators with free-space propagation paths.

5. Conclusions

In conclusion, we have designed a simple THz frequency PIC with a RTR that is capable of frequency engineering, tuning and power modulation. We have exploited longitudinal coupling of electrical field in closely spaced QCL cavities through evanescent field to couple THz light from a ridge into the RTR. The design of the ridge and the RTR was carefully optimized to form a comb of stopbands, which suppress longitudinal modes in the ridge favoring single-mode emission. The device characteristics were modelled using both FEM and an analytical model derived from transfer functions. Two modes of operation have been shown, first the RTR was used as a passive cavity and the drive currents across the ridge was varied to tune the emission frequency through Stark shift of gain. Mode hops over 81 GHz and a change in output power in the range 2–2.75 mW was measured at a constant heat sink temperature of 50 K. Secondly, the output power from the device was varied by ~30% and the frequency tuned by a further 10 GHz when the drive current to the RTR was varied and that across the ridge was invariant.

The results reported here can be improved through further integration of other modular waveguide sections leading to the realization of a THz frequency photonic integrated circuit. The side mode suppression can be increased by coupling of multiple RTRs and by including finite defect site lattices [35]. The side mode suppression can also be improved by reducing the length of the RTR such that the resonant frequencies are separated by integer multiples of the ridge FSR [20]. The divergent output beam profile, typical in metal-metal waveguides due to sub-wavelength confinement, can be improved by integrating planar horn structures at the facets [36,37]. The device complexity can be reduced by using a uniform cavity width of ~48 μm , eliminating the need for tapered sections and reducing the constraint on RTR designs. In such designs, the electrical contacts to the ridge and the RTR can be fabricated using planarization techniques [38].

Funding

Engineering and Physical Sciences Research Council (EP/J017671/1, EP/P021859/1); Royal Society; Wolfson Foundation.

Disclosures

The authors declare no competing interests.

References

1. R. Köhler, A. Tredicucci, F. Beltram, H. E. Beere, E. H. Linfield, A. G. Davies, D. A. Ritchie, R. C. Iotti, and F. Rossi, "Terahertz semiconductor-heterostructure laser," *Nature* **417**(6885), 156–159 (2002).
2. G. Scalari, C. Walther, M. Fischer, R. Terazzi, H. Beere, D. Ritchie, and J. Faist, "THz and sub-THz quantum cascade lasers," *Laser Photonics Rev.* **3**(1-2), 45–66 (2009).
3. L. Li, I. Kundu, P. Dean, E. H. Linfield, and A. G. Davies, "High-power GaAs/AlGaAs quantum cascade lasers with emission in the frequency range 4.7–5.6 THz," presented at the *International Quantum Cascade Lasers School and Workshop*, Cambridge, UK, 2016.
4. L. H. Li, L. Chen, J. R. Freeman, M. Salih, P. Dean, A. G. Davies, and E. H. Linfield, "Multi-Watt high-power THz frequency quantum cascade lasers," *Electron. Lett.* **53**(12), 799–800 (2017).
5. M. Rösch, G. Scalari, M. Beck, and J. Faist, "Octave-spanning semiconductor laser," *Nat. Photonics* **9**(1), 42–47 (2015).
6. L. H. Li, K. Garrasi, I. Kundu, Y. J. Han, M. S. Salih, M. S. Vitiello, A. G. Davies, and E. H. Linfield, "Broadband heterogeneous terahertz frequency quantum cascade laser," *Electron. Lett.* **54**(21), 1229–1231 (2018).

7. L. A. Coldren, "Monolithic tunable diode lasers," *IEEE J. Sel. Top. Quantum Electron.* **6**(6), 988–999 (2000).
8. L. A. Coldren, S. W. Corzine, and M. L. Masanovic, *Diode Lasers and Photonic Integrated Circuits*, 2nd Edition (John Wiley & Sons, 2012).
9. M. S. Vitiello and A. Tredicucci, "Tunable Emission in THz Quantum Cascade Lasers," *IEEE Trans. Terahertz Sci. Technol.* **1**(1), 76–84 (2011).
10. N. Han, A. de Geofroy, D. P. Burghoff, C. W. I. Chan, A. W. M. Lee, J. L. Reno, and Q. Hu, "Broadband all-electronically tunable MEMS terahertz quantum cascade lasers," *Opt. Lett.* **39**(12), 3480–3483 (2014).
11. F. Castellano, V. Bianchi, L. Li, J. Zhu, A. Tredicucci, E. H. Linfield, A. Giles Davies, and M. S. Vitiello, "Tuning a microcavity-coupled terahertz laser," *Appl. Phys. Lett.* **107**(26), 261108 (2015).
12. C. A. Curwen, J. L. Reno, and B. S. Williams, "Broadband continuous single-mode tuning of a short-cavity quantum-cascade VECSEL," *Nat. Photonics* **13**(12), 855–859 (2019).
13. Y. Chassagneux, R. Colombelli, W. Maineults, S. Barbieri, S. P. Khanna, E. H. Linfield, and A. G. Davies, "Predictable surface emission patterns in terahertz photonic-crystal quantum cascade lasers," *Opt. Express* **17**(12), 9491–9502 (2009).
14. A. W. M. Lee, B. S. Williams, S. Kumar, Q. Hu, and J. L. Reno, "Tunable terahertz quantum cascade lasers with external gratings," *Opt. Lett.* **35**(7), 910–912 (2010).
15. S. J. Kindness, D. S. Jessop, B. Wei, R. Wallis, V. S. Kamboj, L. Xiao, Y. Ren, P. Braeuninger-Weimer, A. I. Aria, S. Hofmann, H. E. Beere, D. A. Ritchie, and R. Degl'Innocenti, "External amplitude and frequency modulation of a terahertz quantum cascade laser using metamaterial/graphene devices," *Sci. Rep.* **7**(1), 7657 (2017).
16. D. Turčinková, M. I. Amanti, G. Scaleri, M. Beck, and J. Faist, "Electrically tunable terahertz quantum cascade lasers based on a two-sections interdigitated distributed feedback cavity," *Appl. Phys. Lett.* **106**(13), 131107 (2015).
17. C. Wu, Y. Jin, J. L. Reno, and S. Kumar, "Large static tuning of narrow-beam terahertz plasmonic lasers operating at 78 K," *APL Photonics* **2**(2), 026101 (2017).
18. Y. Ren, D. J. Hayton, J. N. Hovenier, M. Cui, J. R. Gao, T. M. Klapwijk, S. C. Shi, T.-Y. Kao, Q. Hu, and J. L. Reno, "Frequency and amplitude stabilized terahertz quantum cascade laser as local oscillator," *Appl. Phys. Lett.* **101**(10), 101111 (2012).
19. I. Kundu, P. Dean, A. Valavanis, L. Chen, L. Li, J. E. Cunningham, E. H. Linfield, and A. G. Davies, "Discrete Vernier tuning in terahertz quantum cascade lasers using coupled cavities," *Opt. Express* **22**(13), 16595–16605 (2014).
20. I. Kundu, P. Dean, A. Valavanis, L. Chen, L. Li, J. E. Cunningham, E. H. Linfield, and A. G. Davies, "Quasi-continuous frequency tunable terahertz quantum cascade lasers with coupled cavity and integrated photonic lattice," *Opt. Express* **25**(1), 486–496 (2017).
21. I. Kundu, P. Dean, A. Valavanis, J. R. Freeman, M. C. Rosamond, L. Li, Y. Han, E. H. Linfield, and A. G. Davies, "Continuous frequency tuning with near constant output power in coupled Y-branched terahertz quantum cascade lasers with photonic lattice," *ACS Photonics* **5**(7), 2912–2920 (2018).
22. I. Kundu, F. Wang, X. Qi, H. Nong, P. Dean, J. R. Freeman, A. Valavanis, G. Agnew, A. Grier, T. Taimre, L. Li, D. Indjin, J. Mangeney, J. Tignon, S. S. Dhillon, A. D. Rakić, J. E. Cunningham, E. H. Linfield, and A. G. Davies, "Ultrafast switch-on dynamics of frequency tuneable semiconductor lasers," *Nat. Commun.* **9**(1), 3076 (2018).
23. Iman Kundu, Joshua R. Freeman, Paul Dean, Lianhe Li, Edmund H. Linfield, A. Giles Davies, and A. Giles Davies, "Wideband electrically-controlled Vernier frequency tuneable terahertz quantum cascade laser," *ACS Photonics* (to be published).
24. S. Chakraborty, O. Marshall, C. W. Hsin, M. Khairuzzaman, H. Beere, and D. Ritchie, "Discrete mode tuning in terahertz quantum cascade lasers," *Opt. Express* **20**(26), B306–B314 (2012).
25. M. Hempel, B. Röben, L. Schrottke, H.-W. Hübers, and H. T. Grahn, "Fast continuous tuning of terahertz quantum-cascade lasers by rear-facet illumination," *Appl. Phys. Lett.* **108**(19), 191106 (2016).
26. T. Alam, M. Wienold, X. Lü, K. Biermann, L. Schrottke, H. T. Grahn, and H.-W. Hübers, "Wideband, high-resolution terahertz spectroscopy by light-induced frequency tuning of quantum-cascade lasers," *Opt. Express* **27**(4), 5420–5432 (2019).
27. W. Bogaerts, P. De Heyn, T. Van Vaerenbergh, K. De Vos, S. Kumar Selvaraja, T. Claes, P. Dumon, P. Bienstman, D. Van Thourhout, and R. Baets, "Silicon microring resonators," *Laser Photonics Rev.* **6**(1), 47–73 (2012).
28. B. S. Williams, S. Kumar, H. Callebaut, Q. Hu, and J. L. Reno, "Terahertz quantum-cascade laser at $\lambda \approx 100 \mu\text{m}$ using metal waveguide for mode confinement," *Appl. Phys. Lett.* **83**(11), 2124–2126 (2003).
29. Y. Chassagneux, R. Colombelli, W. Maineult, S. Barbieri, H. E. Beere, D. A. Ritchie, S. P. Khanna, E. H. Linfield, and A. G. Davies, "Electrically pumped photonic-crystal terahertz lasers controlled by boundary conditions," *Nature* **457**(7226), 174–178 (2009).
30. S. J. Mason, "Feedback Theory-Further Properties of Signal Flow Graphs," *Proc. IRE* **44**(7), 920–926 (1956).
31. I. Kundu, J. R. Freeman, P. Dean, L. H. Li, E. H. Linfield, and A. G. Davies, "Data associated with "Terahertz photonic integrated circuit for frequency tuning and power modulation","" <http://dx.doi.org/10.5518/756>.
32. A. Yariv, *Quantum Electronics*, 3rd Edition (John Wiley & Sons, 1988).
33. J. Faist, *Quantum Cascade Lasers*, 1st Edition (Oxford University Press, 2013).
34. M. Wienold, L. Schrottke, M. Giehler, R. Hey, W. Anders, and H. T. Grahn, "Low-voltage terahertz quantum-cascade lasers based on LO-phonon-assisted interminiband transitions," *Electron. Lett.* **45**(20), 1030–1031 (2009).

35. I. Kundu, P. Dean, A. Valavanis, L. Li, Y. Han, E. H. Linfield, and A. G. Davies, "Frequency tunability and spectral control in terahertz quantum cascade lasers with phase adjusted finite defect site photonic lattice," *IEEE Trans. Terahertz Sci. Technol.* **7**(4), 360–367 (2017).
36. A. Brewer, J. R. Freeman, P. Cavalie, J. Maysonave, J. Tignon, S. S. Dhillon, H. E. Beere, and D. A. Ritchie, "Coherent detection of metal-metal terahertz quantum cascade lasers with improved emission characteristics," *Appl. Phys. Lett.* **104**(8), 081107 (2014).
37. F. Wang, I. Kundu, L. Chen, L. Li, E. H. Linfield, A. G. Davies, S. Moudji, R. Colombelli, J. Mangeney, J. Tignon, and S. S. Dhillon, "Engineered far-fields of metal-metal terahertz quantum cascade lasers with integrated planar horn structures," *Opt. Express* **24**(3), 2174–2182 (2016).
38. H. Zhang, G. Scalari, J. Faist, L. A. Dunbar, and R. Houdré, "Design and fabrication technology for high performance electrical pumped terahertz photonic crystal band edge lasers with complete photonic band gap," *J. Appl. Phys.* **108**(9), 093104 (2010).